Light Dark Matter eXperiment (LDMX): Letter of Intent

an author[a]

[a]*an institution*

ABSTRACT: The LDMX experiment proposes a high-statistics search for low-mass dark matter at the DASEL beamline using the missing momentum technique, scattering incoming electrons in a tungsten target to produce dark matter via "dark bremsstrahlung". This clear signature is established by individually tagging incoming beam-energy electrons and unambiguously associating them with low energy, moderate transverse-momentum recoils and establishing the absence of a forward-going photon. The primary backgrounds are traditional bremsstrahlung processes with photo-nuclear reactions occurring in the target or forward calorimeter. Therefore, the experiment requires a high-speed, granular calorimeter with MIP sensitivity to identify rare photo nuclear reactions, in addition to low mass tracking that provides high-purity tagging for incoming electrons and clean, efficient reconstruction of recoils. The LDMX concept proposes to meet these challenges by leveraging technology under development for the HL-LHC and experience from the HPS experiment.

Contents

1 Overview and Executive Summary (Editors: Philip Schuster)

The LDMX experiment proposes a high-statistics search for low-mass dark matter at the DASEL beamline using the missing momentum technique, scattering incoming electrons in a tungsten target to produce dark matter via "dark bremsstrahlung". This clear signature is established by individually tagging incoming beam-energy electrons and unambiguously associating them with low energy, moderate transverse-momentum recoils and establishing the absence of a forward-going photon. The primary backgrounds are traditional bremsstrahlung processes with photo-nuclear reactions occurring in the target or forward calorimeter. Therefore, the experiment requires a high-speed, granular calorimeter with MIP sensitivity to identify rare photo nuclear reactions, in addition to low mass tracking that provides high-purity tagging for incoming electrons and clean, efficient reconstruction of recoils. The LDMX concept proposes to meet these challenges by leveraging technology under development for the HL-LHC and experience from the HPS experiment

2 Science Goals (Editors: Philip Schuster, Gordan Krnjaic)

2.1 Testing Thermal Dark Matter

The overwhelming evidence for the existence of dark matter (DM) arises from multiple independent sources. Observations of galactic rotation curves, the power spectrum of the Cosmic Microwave Background (CMB), the cosmological matter power spectrum, light element yields from Big Bang

Nucleosynthesis (BBN), gravitational lensing, and galaxy cluster collisions all require roughly 85% of the matter in our universe to be cold and non-baryonic. Together, these data constitute smoking gun evidence of physics beyond the Standard Model (SM), which contains no viable DM candidate – for a review see [?].

However, despite this impressive body of evidence, the particle nature of DM remains completely unknown; all indications of its existence derive ultimately from its gravitational influence on visible matter in different contexts. Without making any further assumptions about these hypothetical interactions or DM's cosmological history, its viable mass range is wildly unconstrained: 10^{-22} eV – $10 M_\odot$. If DM is lighter than $\sim 10^{-22}$ eV, its Compton wavelength does not fit inside the smallest known DM dominated objects [?] and if it's heavier than $\sim 10 M_\odot$ it would have distorted the CMB power spectrum at early times [?]. Given such an enormous range of viable masses, a realistic DM discovery effort requires a well motivated organizing principle to manageably and systematically test this vast space of possibilities without being narrowly tailored to specific models.

2.1.1 Thermal Origin

A compelling, well motivated organizing principle for the DM search effort is the hypothesis that DM is produced through its interactions with the SM in thermal equilibrium during the early universe. This criterion selects a broad class of popular DM models (including Supersymmetry) and is defined by the requirement that the DM-SM interaction rate exceed the Hubble expansion rate at early times. Once achieved, thermal equilibrium offers some generically attractive features that do not depend sensitively on particular model details:

- **Generically Realized:** Equilibrium is hard to avoid even with tiny coupling constants between dark and visible matter; thus, most *discoverable* models of DM with non-gravitational interactions fall into this category. Alternative mechanisms (e.g. axions produced via misalignment [?] or feebly coupled DM produced via freeze in [?]) require such small couplings that comprehensive experimental probes are prohibitively difficult in most regions of their parameter space – see [?].

- **Minimum Annihilation Rate:** Equilibrium at temperature T populates the DM with a thermal number density $n_{\rm DM} \propto T^3$, which is many orders of magnitude larger than the observed abundance. Thus, viable thermal DM must be depleted with an annihilation cross section $\sigma v \geq 3 \times 10^{-26}$ cm^3/s via the process of thermal "freeze out." This inequality must be saturated (=) if DM is particle/antiparticle symmetric and exceeded (>) if there is an additional primordial DM asymmetry which contributes to the total abundance in addition to the freeze-out component.

- **Narrower Mass Window:** The viable DM mass range becomes much narrower – see Fig. 1. Thermal DM below $\lesssim 10$ keV erases small scale structure in conflict with observation; thermal DM above $\gtrsim 10$ TeV requires nonperturbative and/or non-unitary couplings to realize a sufficiently large annihilation rate.
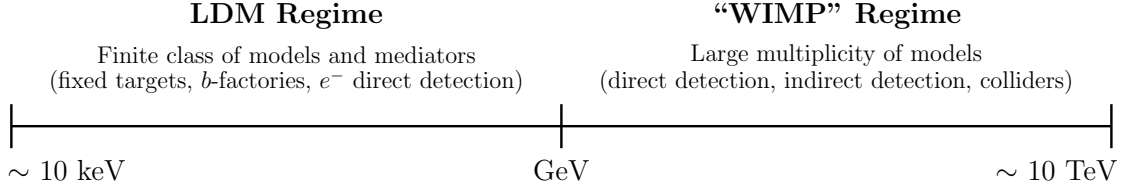
LDM Regime	"WIMP" Regime

Figure 1. The allowed mass range over which DM can thermalize with the SM in the early universe and yield the observed relic abundance via annihilation. For masses below $\lesssim 10$ keV, DM is too hot to form the observed structure of the universe on large scales [**?**] and for masses above $\gtrsim 10$ TeV, a perturbative annihilation rate cannot achieve the correct relic abundance in simple models [**?**].

2.1.2 "WIMP" Dark Matter

If thermal DM is realized in the upper half of the thermal mass window $\sim$ GeV - 10 TeV, it can be a Weakly Interacting Massive Particle (WIMP) charged under the familiar electroweak force and achieve the observed relic abundance by annihilating through via SM gauge interactions. This class of models exploits the numerical coincidence between electroweak-sized cross sections and the requisite annihilation cross section for thermal freeze out $\sigma \sim \alpha^2/m_Z^2 \to \sigma v \sim 3 \times 10^{-26}$ cm^3/s (see [**?**] for a pedagogical treatment). This so-called "WIMP miracle" also naturally arises in popular extensions of the SM that address the electroweak hierarchy problem (e.g. Supersymmetry and extra dimensions) and may even be realized with fifth forces beyond the SM so long as the appropriate coupling-to-mass ratio is of electroweak size, but the latter possibility is not obligatory for masses in the WIMP range.

The discovery techniques available for WIMP and WIMP-like DM are well known and firmly established the experimental community:

- **Direct Detection:** Terrestrial searches for non relativistic WIMP-nucleon scattering in a shielded underground detector [**?**]. This technique is powerful for DM masses near ~ 10 GeV - 10 TeV, but loses sensitivity near the GeV where typical nuclear recoils are $\lesssim$ keV, below detection sensitivity thresholds. The sensitivity of this approach depends critically on the presently unknown DM velocity distribution in the terrestrial neighborhood and is therefore subject to potentially large systematic uncertainties.

- **Indirect Detection:** Typically space based searches of DM annihilation in regions of high DM density (galactic center, dwarf galaxies etc.) [**?**]. This technique is approaching sensitivity to thermal DM annihilation rates for a variety of scenarios, but poorly constrains DM below the few-GeV scale. As with direct detection, the signal strength for indirect detection depends on an unknown DM phase space profile in regions of high density, so the systematic uncertainties of this approach may also be very large.

- **Collider Production** Laboratory based searches for DM produced in association with visible final states in SM particle collisions [**?**]. This technique is powerful and not limited by halo uncertainties or the limitations of non-relativistic scattering off DM particles in the Earth's neighborhood. However, for DM below the GeV scale, the transverse missing energy in a

typical production evennt is too low to impart sufficient recoil P_T to the other visible object(s) in the final state, so sensitivities remain weak for the lower half of the thermal mass window [**?**].

2.1.3 Light Dark Matter (LDM)

Although the thermal freeze-out production mechanism can apply equally well to light DM (LDM) in the keV-GeV range, achieving the observed annihilation rate is no longer possible with SM forces. Annihilation to SM particles via virtual electroweak gauge boson exchange scales as $\sigma v \sim \alpha^2 m_{\rm DM}^2/m_Z^4 \ll 3 \times 10^{-26}$ cm^3/s, which is insufficient for freeze out if $m_{\rm DM} \ll m_Z$. Thus, for light thermal DM to be viable:

- **Light New Forces:** There have to be comparably light force carriers with to mediate an efficient annihilation rate for thermal freeze out.

- **Portals:** Both the DM and the mediator must be singlets under the full SM gauge group; otherwise would have been produced in Z-pole measurements at LEP. Thus, in order for the DM to annihilate away its abundance, the mediator particle must have a *renormalizable*[1] coupling to SM particles through a mass-dimension < 4 singlet "portal" operator built out of SM fields.

The second bullet point sharply constrains the options for LDM mediator particles since the only renormalizable SM operators that satisfy this requirement are

$$\hat{\mathcal{O}}_{\rm portal} = H^\dagger H \ , \ \ HL \ , \ \ B_{\mu\nu} \ , \tag{2.1}$$

and are known respectively as the Higgs, lepton, and vector portals (for a discussion, see [**?**]). Here H is the SM Higgs doublet, L is the SM lepton doublet, and $B_{\mu\nu} = \partial_\mu B_\nu - \partial_\nu B_\mu$ is the $U(1)_Y$ hypercharge field strength tensor, which is independently gauge invariant. Each portal corresponds to a different choice of mediator spin – only a scalar mediator can couple to the $H^\dagger H$ bilinear, only a fermionic mediator can couple to the lepton portal operator LH, and only a spin-1 mediator can couple to the $B_{\mu\nu}$ vector portal. However, for the most predictive model variations, the scalar mediator is strongly disfavored by a variety of experimental constraints [**?**] and the lepton portal interaction is generically proportional to factors of neutrino masses $m_\nu \lesssim 0.1$ eV, so it is difficult to sustain thermal contact between DM and SM sectors. Thus, for the rest of this discussion, we will emphasize the vector portal as the representative mediator1 of LDM interactions.

2.1.4 Predictive LDM Targets

We define the LDM particle to be χ and the mediator to be a "dark photon" A' with lagrangian

$$\mathcal{L} = i\bar{\chi}\displaystyle{\not}\partial\chi + m_\chi\bar{\chi}\chi + g_D A'_\mu\bar{\chi}\gamma^\mu\chi - \frac{1}{4}F'_{\mu\nu}F'^{\mu\nu} + \frac{\epsilon}{2}F'_{\mu\nu}F^{\mu\nu} + \frac{m_{A'}^2}{2}A'_\mu A'^\mu \ , \tag{2.2}$$

---

[1]If the operator were not renormalizable, there would have to be additional, sub-electroweak states integrated out to generate such an interaction since electroweak sized suppression scales in higher dimension operators would reintroduce the overproduction problem. However, the states that UV complete such an interaction would be electroweak charged and ruled out by LEP searches for light, electroweak charged matter.
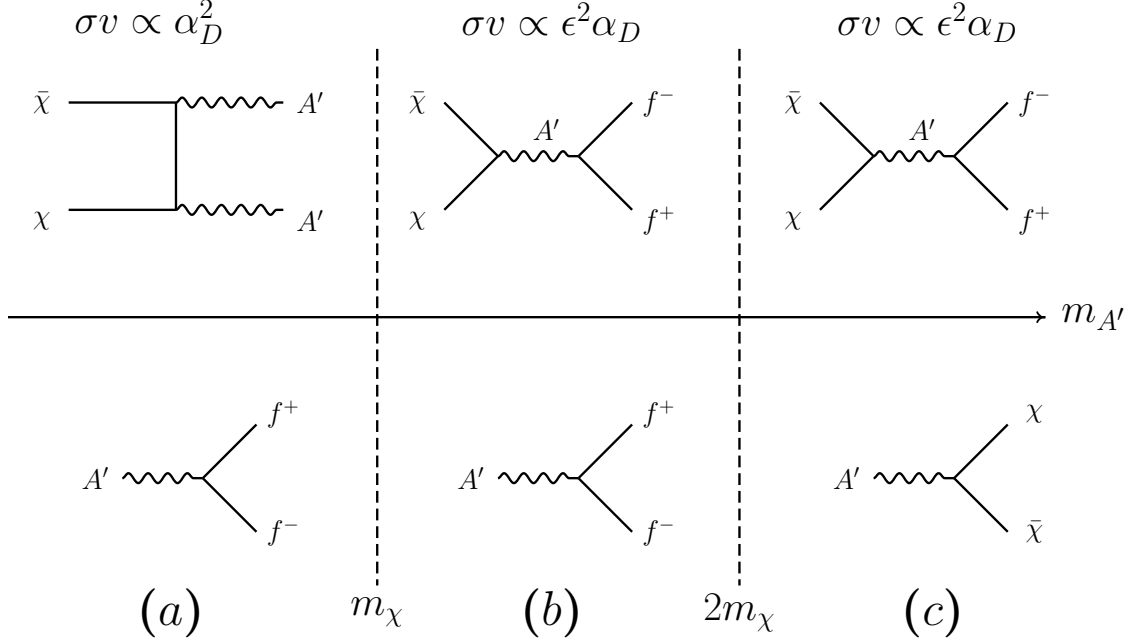
Figure 2. Schematic representation of the different DM annihilation modes (top row) and A' decay modes for $m_\chi/m_{A'}$ ratios. a) Secluded annihilation scenario with a visibly decaying mediator. This scenario has no thermal target and cannot be presented on the y vs. m_χ plane. b) Compressed region with direct annihilation, but a visibly decaying mediator (not considered in this discussion). c) Direct annihilation and invisibly decaying mediator particle.

where $F'_{\mu\nu} = \partial_\mu A'_\nu - \partial_\nu A'_\mu$, $\epsilon \ll$ is the kinetic mixing parameter, which controls A' mixing with the SM photon, and $g_D \equiv \sqrt{4\pi\alpha_D}$ is the A' coupling to the DM. Although we've assumed the DM is a fermion, the qualitative features of this discussion are insensitive to its spin and compatible with scalar candidates as well.

After diagonalizing the kinetic mixing interaction, the dark photon A' acquires a coupling to the SM electromagnetic current

$$\mathcal{L} \to i\bar\chi \slashed\partial \chi + m_\chi \bar\chi\chi + A'_\mu \left(g_D \bar\chi \gamma^\mu \chi + \epsilon e \sum_f Q_f \bar f \gamma^\mu f \right) - \frac{1}{4} F'_{\mu\nu} F'^{\mu\nu} + \frac{m^2_{A'}}{2} A'_\mu A'^\mu , \quad (2.3)$$

where f is a SM fermion and Q_f is its electromagnetic charge.

We distinguish between two distinct annihilation regimes depicted schematically in Fig. 2

- **Secluded Annihilation:** For $m_{A'} < m_\chi$, DM annihilation will predominantly proceed through $\chi\chi \to A'A'$, followed by $A' \to ff$ decays to SM fermions. However, the annihilation rate in this regime is independent of the SM-A' coupling ϵ and therefore difficult to test since thermal freeze out can proceed even for tiny values of ϵ. This regime is depicted on the leftmost column of Fig. 2
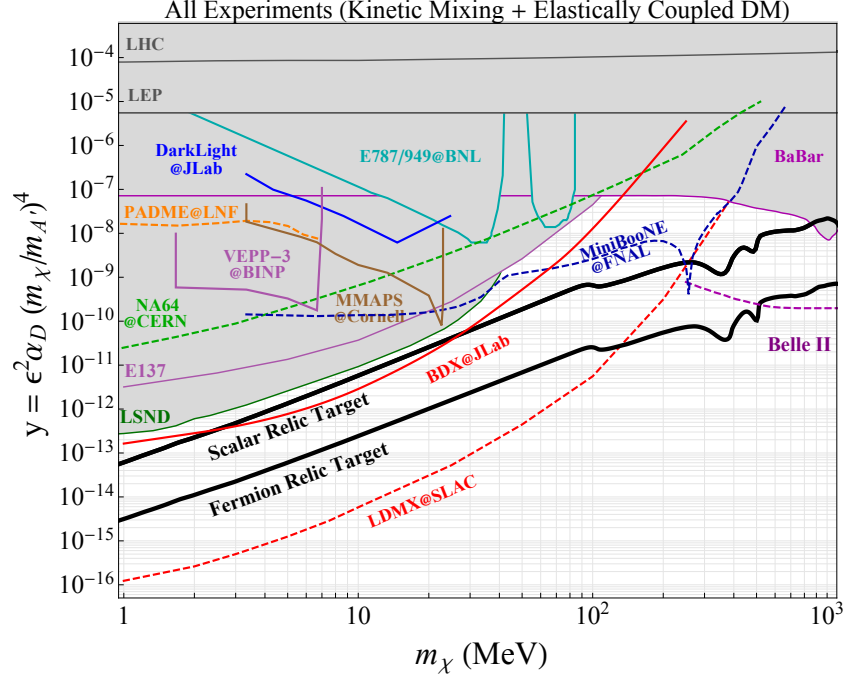
Figure 3. The parameter space for LDM and future experimental projections in the y vs. m_χ plane plotted against the thermal relic targets for scalar and fermion DM – see text for a discussion.

- **Direct Annihilation:** For $m_{A'} > m_\chi$, the mediator decays predominantly to DM and annihilation proceeds via $\chi\chi \to A'^* \to f\bar{f}$ to SM fermions f through a virtual mediator. This regime is depicted in the middle and rightmost column of Fig. 2; ; note the compressed region in the middle column for which $m_\chi < m_{A'} < 2m_\chi$ for which the annihilation rate depends on ϵ but the mediator decay to DM is kinematically forbidden.

Since the cross section for direct annihilation is proportional to all the parameters in the DM lagrangian, it is convenient to define the dimensionless interaction strength y as

$$\sigma v(\chi\chi \to A'^* \to f\bar{f}) \propto \epsilon^2 \alpha_D \frac{m_\chi^2}{m_{A'}^4} = \frac{y}{m_\chi^2} \quad , \quad y \equiv \epsilon^2 \alpha_D \left(\frac{m_\chi}{m_{A'}}\right)^4 \tag{2.4}$$

thus, for each choice of m_χ there is a unique value of y compatible with thermal freeze out independently of the individual values of α_D, ϵ and $m_\chi/m_{A'}$. Reaching experimental sensitivity to this benchmark for masses between $10\,\text{keV} - \text{GeV}$ suffices for decisive coverage of these scenarios.

2.1.5 Current Bounds on LDM

2 Although LDM represent fully half of the viable thermal DM mass range, there has never been a dedicated search for this class of models. Most constraints that apply to the scenarios considered here are reinterpretations (by theorists) of experimental results collected for other purposes and fall into the following categories:

- **CMB Power Spectrum:** LDM can annihilate to SM particles during the time of recombination and ionize the newly formed hydrogen, thereby modifying the CMB power spectrum in conflict with observations from PLANCK [?]. If this annihilation is s-wave and the DM is particle symmetric, the CMB rules out LDM below $\sim$10 GeV. However if the annihilation is p-wave (easily achieved for a scalar DM candidate coupled to a dark photon mediator) or if the DM population is different at the time of CMB (e.g. asymmetric or Majorana inelastic, see [?] for a discussion)

- **Colliders:** Although high energy colliders (LHC, Tevatron, LEP) generally have poor sensitivity to LDM, high intensity B-factories can perform analogous searches for $e^+e^- \to \gamma A'$ production and set impressive constraints in the 100 MeV - few GeV mass range.

- **Beam Dumps:** The LSND proton beam dump experiment [?] is sensitive to LDM production and scattering in their measurement of the electron-neutrino neutral current cross section. At LSND, DM can be produced in pion decays $\pi^0 \to \gamma A' \to \gamma \chi \chi$ and subsequently scatter in a downstream detector. The E137 electron beam dump experiment to search for axion like particles is also sensitive to similar processes in which DM is relativistically produced through the kinetic mixing interaction in the beam dump, passes through a downstream detector and deposits electromagnetic energy by scattering off detector targets [?].

- **Rare Kaon Decays**: LDM can also be produced in rare Kaon decays $K^+ \to \pi^+ A' \to \pi^+ \chi \chi$ which can contribute to the signal region of E787/E949 [? ?] which measured the $K^+ \to \pi^+ \bar{\nu} \nu$ branching ratio.

- **Electron Direct Detection**: The results of XENON10 S2-only study of electron recoil signals can be used to constrain LDM that scatters elastically off detector electrons [?]. Although the backgrounds for this sample are not well understood, a conservative extraction of the DM scattering limit can be used to constrain this parameter space. This bound is competitive with E137 and E787/E949 in Fig. **??**, but is slightly covered by those constraints for the benchmarks presented, so it is not shown.

These constraints are collected in on the y vs m_χ parameter space depicted in Fig. 3 alongside projections for Belle II [?], BDX [? ?], MiniBooNE [?], NA64 [?], VEPP-3 [?], and MMAPS [?]. Also shown are the thermal targets for fermion and scalar LDM candidates, which are invariant in this parameter space regardless of what assumptions about ϵ, α_D, and $m_\chi/m_{A'}$ we choose. However, the other constraints on this parameter space are not necessarily invariant in this way (e.g. collider production only depends on ϵ), so the shaded regions in Fig. 3 represent the most conservative versions of these constraints for which these parameters are chosen to reveal all the remaining gaps in the parameter space consistent with the assumption of direct annihilation.

This plot illustrates the large, orders of magnitude gaps in coverage between existing (and projected) constraints and the thermal relic contours for LDM. In order to decisively cover thermal LDM in the direct annihilation regime, a dedicated effort will be required. To this end, we also show the

projections for LDMX@SLAC, which is the only proposed effort to probe the thermal target for both scalars and fermions down to the MeV range.

2.2 Nuclear Physics Measurements

Work in progress...

3 Detector Concept

Basic Considerations and Overview

- Signal characteristics

- Possible backgrounds

- Achieving high luminosity

- Explain why we want a tagger tracker, moderate 0.1 X0 target, recoil tracker, high granularity calorimeter, hadronic veto

- Summarize the overall layout of the experiment

3.1 Beamline (Editors: Tim Nelson, Omar Moreno)

The LDMX beamline is relatively simple, consisting only of an analyzing magnet and a vacuum chamber into which the tagging and recoil trackers are installed. The analyzing magnet is a common 18D36 dipole magnet with a 14-inch vertical gap and operated at a central field of 1.5 T. A stainless-steel vacuum chamber with 1/2" walls fits just inside the magnet bore supporting the tracking detectors and their readout electronics. The upstream end of the vacuum chamber is closed by a plate with a 6" conflat flange for connection to the upstream beampipe and the downstream end is closed by a titanium vacuum window in front of the ECal face which sits 20 cm downstream of the target at roughly the same z position as the outer face of the magnet coils. The magnet is rotated by approximately 100 mrad about the vertical axis with respect to the upstream beamline so that the incoming 4 GeV beam follows the desired trajectory to the target, with the incoming beam arriving at normal incidence to, and centered on, the target which is laterally centered in the vacuum chamber at z=40 cm relative to the center of the magnet. Although the specific dimensions differ, this arrangement (aside from the vacuum window) is very similar to the magnet and vacuum chamber employed by the HPS experiment at JLab. As with HPS, additional vacuum boxes at the upstream end will be appended to the vacuum chamber as needed to accommodate feedthroughs for power, readout and cooling.

A number of 18D36 magnets, not currently in use, are in hand at SLAC along with the steel required to adjust the magnet gap, if required to suit our purposes. These include a magnet that is already assembled with a 14-inch gap as planned for LDMX. This magnet was tested to 1.0 T in 1978 at which the power dissipated was 199 kW. Based on the current capacity of the other similar magnets with smaller gaps, it is expected that this magnet can be operated at 1.5 T, resulting in a power dissipation of approximately 450 kW and requiring approximately 55 gpm flow of cooling water. If this magnet proves to be suitable for LDMX, it will simply have to be split, cleaned up, reassembled before testing and carefully mapping the field in the tracking volumes.

Since End Station A (ESA) is relatively distant from the critical areas in the Beam Switchyard, the vacuum requirements in ESA are quite modest: roughly 10^{-4} Torr or better. Therefore, standard vacuum fabrication techniques for the vacuum chamber and vacuum window will clearly suffice here. Furthermore, since HPS has achieved better than 10^{-5} Torr at JLab, it is clear that the construction

techniques developed there will work here as well. However, as with HPS, a system of monitoring and interlocks capable of closing automatically controlled vacuum valves will be required to ensure that the liquid cooling system of the trackers cannot spoil the beam vacuum.

Although the final location of LDMX has not been determined, the upstream end of the ESA beamline has the most room and best access for locating the relatively large apparatus. In particular, there is a suitable concrete pedestal for mounting the dipole with sufficient room on all sides to support the calorimeters and accommodate the required beamline elements.

3.2 Overview of Tracking and Target Systems (Editors: Tim Nelson, Omar Moreno)

Although the tagging and recoil trackers function as two distinct systems, they use common technologies and share the same support structures and data acquisition hardware. In particular, the first four layers of the recoil tracker are identical to the layers of the tagging tracker and share the same support and cooling structure. The key element of this upstream support structure is a vertically-oriented aluminum plate onto which the stereo modules are mounted. To provide cooling, a copper tube is pressed into a machined groove in the plate through which coolant flows. This support plate slides from the upstream end of the vacuum chamber into precision kinematic mounts in a support box that is aligned to and locked in place inside the vacuum chamber. Another similar plate slides into the support frame on the positron side of the chamber which hosts the Front End Boards (FEBs) that distribute power and control signals from the DAQ and digitize raw data from the modules for transfer to the external DAQ. The last two layers of the recoil tracker, being much larger, are supported on another structure; a cooled support ring onto which the single-sided, axial-only modules are mounted. This support ring is installed from the downstream end of the chamber, engaging precision kinematic mounts in the support box for precise alignment to the upstream stereo modules. The cooling lines for all three cooled structures; the upstream and downstream tracker supports and the FEB support; are routed to a cooling manifold at the upstream end of the vacuum chamber which, in turn, connects to a cooling feedthrough with dielectric breaks on the bottom of the vacuum box.

It is the interposition of the target between the last layer of the tagging tracker and the first layer of the recoil tracker that clearly distinguishes between the target and recoil tracking systems. The target is a 350 micron tungsten sheet, comprising 10% of a radiation length. This choice of thickness provides a good balance between signal rate and transverse momentum transfer due to multiple scattering which limits the utility of using transverse momentum as a signal discriminator. The tungsten sheet is glued to a 1 mm sheet of PVT scintillator which provides a fast level-0 signal to the ECal trigger indicating the passage of a beam electron in a given beam pulse. The scintillator-tungsten sandwich is mounted in an aluminum frame which can be inserted into the upstream tracker support plate from the positron side to simplify the process of replacing or swapping the target. With the scintillator mounted on the downstream face of the target, it can also be used to help identify events where a bremsstrahlung photon has undergone a photonuclear reaction in the target.

3.3 Tagging Tracker (Editors: Tim Nelson, Omar Moreno)

The tagger tracker is designed to unambiguously identify incoming beam electrons with the correct energy and precisely determine their momentum, direction, and impact position at the target. The

key elements of the design are determined by this goal. First, the long, narrow layout of the tagger tracker accepts only beam electrons that have the roughly the momentum and trajectory expected for the incoming beam to eliminate any off-energy beam electrons. Second the layers have low mass and are spaced far apart in a significant magnetic field to ensure a precise estimate of momentum. Finally, a large number of layers ensures the redundancy required to ensure high-purity pattern recognition.

The layout of the tagging tracker is summarized in Table XXX. The tagging tracker consists of six double-sided modules of silicon microstrips arranged at 10 cm intervals upstream of the target, with the first module centered at z=-7.5 mm. The modules are positioned laterally in the vacuum chamber so that they are centered along the path of incoming 4 GeV beam electrons.

Each module places a pair of 4 cm × 10 cm sensors back to back; one sensor with vertically oriented strips for the best momentum resolution and the other at 100 mrad stereo angle to improve pattern recognition and provide three-dimensional tracking. The sensors are standard p^+-in-n type silicon microstrip sensors identical to those used for HPS. These sensors have 30(60) μm sense(readout) pitch to provide excellent spatial resolution at high S/N ratios and are operable to at least 350V bias for radiation tolerance.

The sensors are read out with CMS APV25 ASICs operated in multi-peak mode, which allows for reconstruction of hit time with a resolution of approximately 2 ns. At very high occupancies, six sample readout can be used to distinguish hits that overlap in time down to 50 ns, which limits the readout rate, and therefore the trigger rate, to approximately 50 kHz. However, at lower occupancies as anticipated at LDMX, three-sample readout may suffice, enabling a maximum trigger rate approaching 100 kHz. These sensors are mounted on standard FR4 hybrid circuit boards which provide the power conditioning and I^2C control for the APV25, as well as a thermal path to the cooled support structure.

The sensors and hybrids are assembled into half-modules, which are the smallest non-rebuildable units of the tagger tracker. Each half module consists of a single sensor, glued to the hybrid at one end with conductive epoxy to provide bias voltage and support. A thin ceramic plate is glued to the other end of the sensor for support. A pair of half modules is attached to either side of an aluminum module support with screws to form a module. A vacuum compatible thermal compound between the half-module and the support ensures a good cooling path. Finally these double-sided modules are attached to the upstream support plate described in Section XXX to position them along the beamline. This support arrangement places only silicon in the tracking volume and no material on the side of the tagger towards which electrons bend to eliminate secondaries that would be generated by degraded beam electrons hitting material close to the tracking planes.

Overall, this design is similar to that of the HPS tracker with some important simplifications. First, because the radiation dose here is modest, cooling is only needed to remove heat from the APV25 chips and not to keep the silicon itself cold. Therefore, water cooling close to room temperature can be used and the significant issues of differential thermal expansion can be ignored. Second, the detector here is in no danger from the nominal beam, so it does not need to be remotely movable as in HPS. Finally, the vacuum chamber here is of a very generous size to achieve the desired acceptance in the ECal and recoil tracker, so the vacuum chamber is not crowded, as is the case with HPS. In summary, the tagger tracker is nearly identical to, but is a significant simplification of, the tracking

system built for the HPS experiment. For this reason, the risk associated with this project is small.

3.4 Recoil Tracker (Editors: Tim Nelson, Omar Moreno)

The recoil tracker is designed to identify low-momentum (50 MeV - 1.2 GeV) recoils and precisely determine their momentum, direction and impact position at the target. In addition, it must work together with the calorimeters to correctly distinguish low-momentum signal recoils from scattered beam electrons and multi-particle backgrounds. The key elements of the design are determined by this goal. First, the recoil tracker is placed at the end of the magnet in the beginning of the fringe field to optimize tracking for particles up to two orders of magnitude softer than the beam energy electrons measured by the tagging tracker. Second, the recoil tracker is short and wide for good acceptance in angle and momentum and to minimize the distance from the target to the calorimeters to improve their angular coverage. Finally, the recoil tracker provides 3-d tracking near the target for both direction and impact parameter resolution but emphasizes low mass density over the longest possible lever arm further downstream to deliver the best possible momentum resolution. This design delivers good momentum resolution for both multiple-scattering limited low-momentum tracks and beam energy electrons that are nearly straight in the fringe field.

The layout of the recoil tracker is summarized in Table XXX and consists of four stereo layers immediately downstream of the target and two axial layers at larger intervals in front the the ECal. The stereo layers are double-sided modules of silicon microstrips arranged at 15 mm intervals downstream of the target, with the first module centered at z=+7.5 mm. These modules are laterally centered on the target and the center of the vacuum chamber and are identical to the modules of tagger tracker that are mounted upstream on the same support plate.

The thinner axial-only layers, at z=+90 mm and z=+180 mm, are mounted on a separate support structure at the downstream end of the vacuum chamber as described in Section XXX and have a somewhat different module design. Each module consists of a pair of sensors, glued end-to-end, with an APV25-based FR4 hybrid circuit board at each end of this structure to read out the two sensors. The sensors are standard p^+-in-n silicon microstrip sensors, but are somewhat shorter and wider than those used in the stereo modules and therefore require six APV25 chips to read out each sensor instead of five. The modules are supported at both ends by screw attachment of the hybrids to castellated support blocks attached to the cooled support structure. A vacuum compatible thermal compound is used to ensure good thermal conductivity between the hybrid and the support structure.

3.5 Forward Electromagnetic Calorimeter (Editors: Joe Incandela)

3.6 Hadronic Veto System (Editors: Jeremy Mans, Nhan Tran, Andrew Whitbeck)

It is also important to extend the calorimeter to veto neutral hadrons being produced in photo-nuclear reactions. As exclusive reactions of this type are rare, the rates and radiation doses will be much lower as the design for the HG calorimeter is designed to fully contain the electromagnetic showers. This removes the requirement for silicon in the hadronic calorimeter section. A scintillator-based sampling calorimeter is a natural solution in this situation. The goal of the hadronic veto system is to identify neutral hadrons in the energy range from above approximately 100 MeV to several GeV with high

efficiency. This requires a hadronic calorimeter with at least 5 nuclear interactions of depth in order to fully contain the most energetic of neutrons with greater than 99% probability. Simultaneously, in order to detect lower energy neutrons, absorbing layers cannot be too thick such that neutrons of hundreds of MeV are captured in the absorbers. Therefore, a steel-scintillator (polystyrene) calorimeter of approximately 15 layers and totaling 5 nuclear interaction lengths is proposed. Each layer is structured as 50 mm of Steel, 2 mm air gap, 6 mm of scintillator, and 2 mm of air gap where the air gaps are left for detector services. The transverse size of each layer is 1 x 1 m to cover the solid angle of the signal acceptance. Transverse granularity of the system is not required due to the lower rates expected in the hadronic system and in order to maintain high efficiency for neutral hadron detection. An illustration of the hadronic veto system is given in Fig. 4.

Figure 4. Placeholder... Drawing of HCAL, is it needed? Could be integrated into a full detector rendering

Fast readout is also required of the hadronic calorimeter system in order to coincide with electromagnetic calorimeter information. Readout will be based on the CMS Phase 1 upgrade HCAL system which has fast readout capabilities intrinsically at frequencies of 40 MHz and would be sufficient for the DASEL beam structure. Scintillating light is read out by wavelength shifting fibers with silicon photomultipliers (SiPMs) as the photodetectors. SiPM technology is chosen due to high gain and low noise capabilities. Each layer is read out by N wavelength shifting fibers and the light is optically summed into M photodetectors In addition to the SiPMs, readout modules (48/64 channels per) and charge integration electronics designed for the CMS detector can be re-purposed for the LDMX experiment with minimal changes and takes advantage of experience of CMS collaborators on LDMX. The timescale for commissioning of the readout electrons in CMS are 2017/2018 and thus are appropriate for the LDMX timeline.

3.7 Wide-Angle Calorimeter ??

3.8 Trigger System (Editors: Jeremy Mans, Nhan Tran, Andrew Whitbeck)

The LDMX trigger system is designed to reduce the typical beam particle arrival rate of 46 MHz to a rate of 5 kHz for storage and analysis. The selection is performed by a combination of dedicated hardware and software running on general-purpose computers.

The first stage trigger is implemented in hardware and allows the selection of both candidate events for dark matter production and important samples for calibration and detector performance monitoring. The overall trigger management is provided by a trigger manager board, which receives inputs from the various triggering subsystems including the silicon calorimeter and the scintillator calorimeter. The latency requirements on the trigger calculation latency are set by the tracker readout ASIC to 2us.

The primary physics trigger is based on the silicon calorimeter and is designed to select events with energy deposition significantly lower than the full beam energy. The silicon calorimeter ASIC calculates the total energy in 2x2 fundamental cells for every 46 MHz bucket. The energy information

Figure 5. Drawing of the trigger fiber hodoscope

is transferred by digital data link to the periphery of the calorimeter, where sums can be made over larger regions and transferred by optical link to the trigger electronics. The total energy is then used to select the events.

The use of a calorimeter trigger requirement of energy below a threshold also requires a beam-presence measurement to avoid very high trigger rates during crossings where there is no beam electron present. The trigger fiber hodoscope is designed to serve this purpose. The hodoscope is constructed of an array of 1 mm-diameter scintillating fibers, which are mounted immediately upstream of the tungsten target. [more details on the mechanics, including orientation of the fibers]

The fibers from the hodoscope are brought to an optical vacuum feedthrough and a clear fiber ribbon is connected on the outside of feedthrough to carry the light signals to the readout electronics. Based on studies by the LHCb collaboration[**?**], scaled to the diameter of fibers in use for the hodoscope, we expect a typical signal of [] photons to be produced in the hodoscope by a beam electron after a total absorbed radiation dose of XXX Gray. We expect to able to bring at least [50%] of these photons to the readout SiPMs.

The same electronics design is used for readout of the hodoscope and the scintillator calorimeter. This readout is based on SiPMs and the housing is designed to allow operation of the SiPMs at reduced temperatures (below $5°C$) to reduce the thermally-induced single-photon noise. The typical photodetector efficiency of these SiPMs is [30%][**?**], providing a typical signal of [] PEs in the electronics. The readout electronics will continuously digitize the SiPM signal, providing an integrated charge as well as time-of-arrival measurement for the pulse with an LSB of 500 ps. Both amplitude and timing information can be provided to the trigger, allowing the correction of the calorimeter amplitude for timewalk effects already at trigger level.

3.9 DAQ (Editors: Jeremy Mans, Nhan Tran, Andrew Whitbeck)

4 Physics and Detector Simulation

Simulations Overview (Editors: Natalia Toro, Jeremy McCormick)

This section describes the methods used to simulate signal and background physics reactions and the responses of various detectors to these reactions. For historical reasons, two separate simulation frameworks have been used: the "tracker simulation" implemented in SLIC comprises a full simulation of the tagger tracker and recoil tracker, with ECAL material included but not its detector response. Likewise, the "calorimeter simulation" implemented directly in Geant4 comprises a full simulation of the ECAL and HCAL, with recoil tracker material included upstream. In both cases, the target material and magnetic field map are also included. Please check for accuracy These two simulations are described in more detail in §??–??.

While the primary simulation engine is Geant4 [?], the signal reaction (Dark Matter pair production) is modelled using an external generator based on MadGraph/MadEvent4 [?]. This generator, its validation, and the interface with Geant4 are described in §??. All background processes are modelled directly in Geant4, with modifications and biasing for photonuclear processes as discussed in §??.

4.1 Simulation of the Tagger and Recoil Trackers (Editors: Omar Moreno, Jeremy McCormick)

The simulation of the passage of both charged and neutral particles through both the tagger and recoil trackers uses a software package based on SLAC's org.lcsim infrastructure which wraps Geant4. The simulation creates realistic charge depositions in the silicon layers, simulates the APV25 readout chip amplifier chain as well as the 24 ns sampling of the signal, creates clusters and performs track finding. The performance studies assumed that the tagger (recoil) tracker is within a uniform dipole field of strength -1.5 T (-.75 T), while all acceptance studies use the full field map. A rendering of the tagger and recoil tracker as used in the simulation is shown on Figure **??**.

4.1.1 Readout simulation

4.1.2 Hit Reconstruction

The six samples emerging from each channel are fit using the following 3-pole function

$$f(t) = A \frac{\tau_1^2}{(\tau_1 - \tau_2)^3} \left(e^{-\frac{t-t_0}{\tau_1}} - \sum_{k=0}^{2} \left(\frac{\tau_1 - \tau_2}{\tau_1 \tau_2} (t - t_0) \right)^k \frac{e^{-\frac{t-t_0}{\tau_2}}}{k!} \right) \tag{4.1}$$

where τ_1 and τ_2 represent the fall and rise time of the shaper signal respectively. The amplitude, A, and the time of the hit, t_0, are then determined from the fit.

Hits on neighboring strips are clustered using a nearest neighbor algorithm as follows:

- A list of seeds is created from all raw hits that have an amplitude, S, $> 4 \times \sigma_{\text{Noise}}$

- Recursively add neighboring strips that have $S > 3 \times \sigma_{\text{Noise}}$ until a strip with $S < 3 \times \sigma_{\text{Noise}}$ is found.

- Require that neighboring hits have a t_0 that is within 8 ns of the seed hit.

- Repeat the first two steps until seed strips are no longer found.

- Require that a cluster has an amplitude $> 4 \times \sigma_{\text{Noise}}$.

After hits on a sensor have been clustered, the cluster time is computed as the amplitude-weighted average of the t_0 times from the hits that compose it. All clusters in adjacent pairs of layers are combined to create 3D hits.

4.1.3 Track Reconstruction

The track finding and fitting algorithm proceeds in steps following a specific "tracking strategy". The strategies outline which layers are used, the minimum number of hits required to form a track and kinematic constraints. The algorithm proceeds as follows:

- All possible combinations of hits are formed from the seed layers and and a helix fit is performed. Only those seeds which satisfy a χ^2 requirement are kept.

- Once all seeds have been found, hits from a specified "confirm" layer are added to the seeds and a helix fit is performed once again. Those fits which do satisfy a χ^2 cut are eliminated.

- Finally, tracks are "extended" by hits from the rest of the layers. After the addition of a hit, a helix fit is performed. If the track fails the χ^2 constraint, the hit is discarded. This procedure is repeated until all hits in a layer have been added to all seeds, however, it is possible for all hits in a layer to be discarded.

- All track candidates are merged in order to form a set of unique tracks. Tracks are allowed to share at most one hit. If a pair of tracks shares more than a single hit, the track with the best chi^2 is chosen.

Need to talk about what strategy and cuts are being used.

4.2 Simulation of the Calorimetry Systems (Editors: Owen Colegrove, Joe Incandela)

A common simulation framework is utilized for the electromagnetic and hadronic calorimeter systems based solely on `GEANT4`. In addition to a full implementation of the sampling layers for both calorimeters, the target, recoil tracker and magnetic field are also included.

4.2.1 Digitization of Forward Electromagnetic Calorimeter

add stuff here, make it common with trigger description?

4.2.2 Digitiztaion of the Hadronic Veto System (Editors: Nhan Tran, Andrew Whitbeck)

After full `GEANT4` simulation, we simulate the digitization of the particle-level interactions in our detector to understand how well we can reconstruct events in the hadronic calorimeter. Given the particle-level energy deposition per layer, we can convert that into the number of minimum ionizing particles (MIP) that we expect in that layer. The translation comes by first estimating the typical

energies deposited in a calorimeter model for a MIP. This can be seen in Fig. 6 where a distribution of energies deposited in a given layer is shown for a single MIP muon.

By translating the energy deposited into a single layer, we can compute how many MIPs we expect in a given layer in a given event. From CMS testbeam studies [], it is computed that 1 MIP corresponds to about 13.5 photo-electrons measured in the SiPM. We then set the threshold for a layer becoming vetoed in our detector simulation based on number of photo-electrons measured in the SiPM That threshold is set at 9 photo-electrons which is $> 4\sigma$ above the typical noise in SiPMs which is typically 2 photo-electrons.
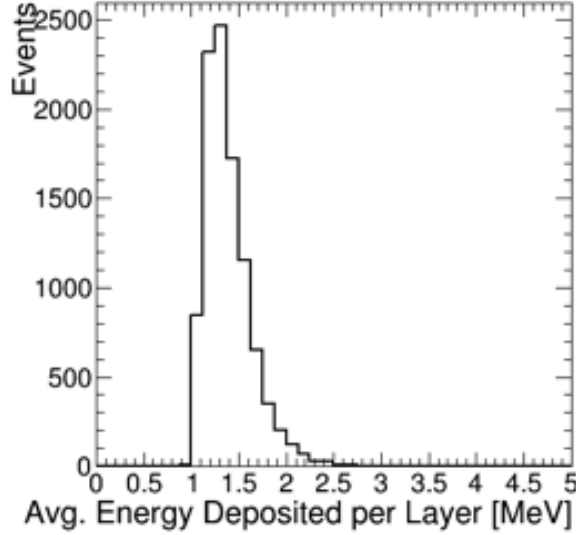

Figure 6. Distribution of energies deposited in scintillator from muon to characterize MIP behavior in plastic scintillator

4.3 External Physics Generator for Signal Reaction (Dark Matter Production) (Editor: Natalia Toro)

While background processes are modelled entirely in the Geant4 framework, the new physics of Dark Matter production is modelled using an external event generator based on MadGraph/MadEvent4 [**?**]. Here we describe this generator, its validation, and the interface with Geant4.

MadGraph is an automated tool for calculating the tree-level amplitudes for arbitrary physics processes, which allows users to define Feynman rules for new physics models; MadEvent is a Monte Carlo event generator based on MadGraph. MadGraph/MadEvent4 (MG/ME) was designed for the study of high-energy collider reactions, but minor modifications to the code (introducing non-zero masses for incident particles and for the electron, and an electromagnetic form factor as described in [**?**] for the nucleus) allow for its application to fixed-target processes. These modifications and a new-physics model that introduces a dark photon with arbitrary mass and kinetic mixing ϵ with the photon has been used for the APEX test run [**?**] and HPS experiment [**?**]. For LDMX, we have

added light dark matter particles (either fermions or scalars) that couple to the dark photon with an arbitrary interaction strength g_D. This allows us to simulate the signal process of DM particle pair-production via either decay of an on-shell A' or off-shell A' exchange. This report focuses on the on-shell production process, though the kinematics of the two are very similar.

Do we want to say something explicit about the form factors?

Within MG/ME, we generate events for the DM production process $e^- W \to e^- W (A' \to \chi \bar{\chi})$ where χ represents the dark matter particle and $\bar{\chi}$ its antiparticle. Events are generated assuming a 4 GeV incident electron and Tungsten nucleus at rest as the initial state. MG/ME computes a Monte Carlo approximation of the inclusive cross-section for this process, and generates a sample of unweighted events in the Les Houches Event (LHE) format [**?**]. The inclusive cross-section computed by MadGraph is stable within 1% and is consistent within $\sim 30\%$ with independent calculation of the cross-section in the Weizsacker-Williams (WW) approximation from [**?**]. The deviations from the WW inclusive cross-section are largest at high and low masses, and compatible with the size of errors expected in the WW approximation.

[IS THSI RIGHT?] To seed Geant4 events from the MG/ME output, we read the four-momentum of the recoiling electron and Tungsten nucleus?? from the LHE file and use these to populate an STDHEP event. The electron and nucleus are assumed to originate from a common vertex, uniformly distributed over the thickness of the target and over a transverse region spanning **CHECK!** ± 1 **cm in the** x **direction and** ± 2 **cm in the** y **direction about the nominal center of the target.**

4.4 Photonuclear Model and Biasing (Editors: Natalia Toro, Omar Moreno)

5 Performance Studies

Baseline luminosity: We want to handle 4×10^{14} electrons on target (EOT) with incoming energy of 4 GeV.

5.1 Signal Characteristics and Selection Strategy

Please note that we need to optimize the energy selection used below. Starting definition:

Tracking:

- One incoming beam electron with E_{beam} close to 4 GeV and a well measured trajectory.

- Quality cuts (as needed) to reduce any dangerous brem (or photo-nuclear) reactions in the tagger tracker material

- One recoiling electron with $E \lesssim 1.2$ GeV that points back to the incoming beam electron track.

- An activity cut in the recoil tracker to reject photo-nuclear reactions in the target

- An inferred "missing momentum" trajectory and magnitude

Calorimetry:

- One soft recoil shower with $E \lesssim 1.2$ GeV that is consistent with recoil tracker trajectory

- An activity cut in the "missing momentum" region for the ECal

- An explicit veto on energetic (energy range needs to be specified) hadrons in both the ECal and hadron veto system

5.2 Tagging Tracker Performance (Editors: Tim Nelson, Omar Moreno)

The tagging tracker must identify incoming beam-energy electrons with extremely high purity, suppressing the mis-reconstruction of any incoming low-momentum charged particles as beam energy electrons. In particular, any incoming charged particle within the recoil acceptance for signal that is reconstructed as having the beam energy in the tagging tracker is an irreducible background. The design of the tagging tracker makes the likelihood of such errors vanishingly small, with good resolution for both beam energy and off-energy incoming tracks and an exceedingly low rate of mis-reconstruction for tracks within the recoil energy acceptance.

In order for an incoming low momentum particle to fake a beam energy electron in the tagger, a number of conditions must simultaneously be met:

1. The incoming particle must reach the first tagger layer or it will not intersect with any material until it hits the wall of the vacuum chamber.

2. The particle must either scatter in each layer in order to fake a 4 GeV track or create secondaries that generate occupancy which confuses the pattern recognition in the tracker resulting in reconstruction of a fake 4 GeV track.

3. The resulting track must have a trajectory consistent with that of a typical 4 GeV beam electron all the way through the tracker.

4. The resulting track must have an impact point at the target consistent with a reconstructed track within the signal acceptance in the recoil tracker.

Using an analytic model of the tagging tracker that includes the effect of intrinsic resolutions and multiple scattering in the tracker planes, it is evident that each of these requirements places a very heavy penalty on any off-energy component in the beam. First, incoming particles with less than approximately 500 MeV momentum will not hit the first layer of the tagger unless they are significantly off-trajectory as well. Furthermore, even at 500 MeV, a first scatter of more than $10°$ is needed in order for the incoming particle to appear to be on the correct trajectory. It is clear then that the most challenging scenario is large contamination with incoming charged particles at the top of the momentum range for signal recoils, nominally 1.2 GeV. Such particles have the highest likelihood of reaching the first layer of the tagger tracker without being bent away by the magnetic field and require much smaller scatters and/or track reconstruction errors to result in fake tags. In order for a 1.2 GeV particle to make a trajectory through the tracker consistent with a 4 GeV track, six successive scatters of approximately ten milliradians must occur, each equivalent to approximately 15σ on the multiple scattering distribution. From the tails of the Moliere scattering distribution, the likelihood of each of these scatters is smaller than one per million. Therefore, the much more likely scenario is the generation of secondaries an the material of the tagger tracker followed by misreconstruction of a fake 4 GeV track. Since the resulting 4 GeV track must arrive at the target on the correct trajectory and beam energy electrons arrive normal to the target with a one-sigma error of 250 microradians, there is very little phase space for randomly reconstructed 4 GeV fakes to have the correct trajectory. Finally, any falsely reconstructed 4 GeV track must have a common impact point in the target with a real track of matching momentum in the recoil tracker, which is unlikely for a falsely reconstructed tracks.

In order to more fully test these scenarios, two samples of incident electrons were simulated and reconstructed in the tagger tracker. The first is a sample of XXX 4 GeV electrons on the nominal beam trajectory. The second is a sample of XXX 1.2 GeV electrons on a trajectory that allows them to pass through all seven layers of the tagging tracker. The 4 GeV sample confirms the expected resolutions, as shown in Figures **??**.

These indicate that tight requirements can be made in both the energy and trajectory at the target that rejects off-momentum particles that could be present in the incoming beam and that the tagging tracker identifies a precise impact position that can be used for tracking recoil candidates. The 1.2 GeV sample confirms at the level of 1 part in $10^{?}$ that these tracks cannot be mistaken for 4 GeV tracks, as shown in Figure 9. In order to probe the likelihood of reconstructing fake 4 GeV tracks at higher statistics we further introduce random noise hits on all planes of the tracker at rates of 10^{-3}, 10^{-2} and 10^{-1} in all planes of the tracker, where typical noise occupancies in similar HPS modules are roughy 10^{-4}. Figure 10 shows the resulting distribution of reconstructed tracks in energy and p_T at the target. Obviously, such extreme occupancies in the tracker are atypical, and would easily be selected against with negligible impact on signal efficiency. Furthermore, these fake tracks, not being due to an individual low-momentum track, will typically not align with a low-momentum track in the
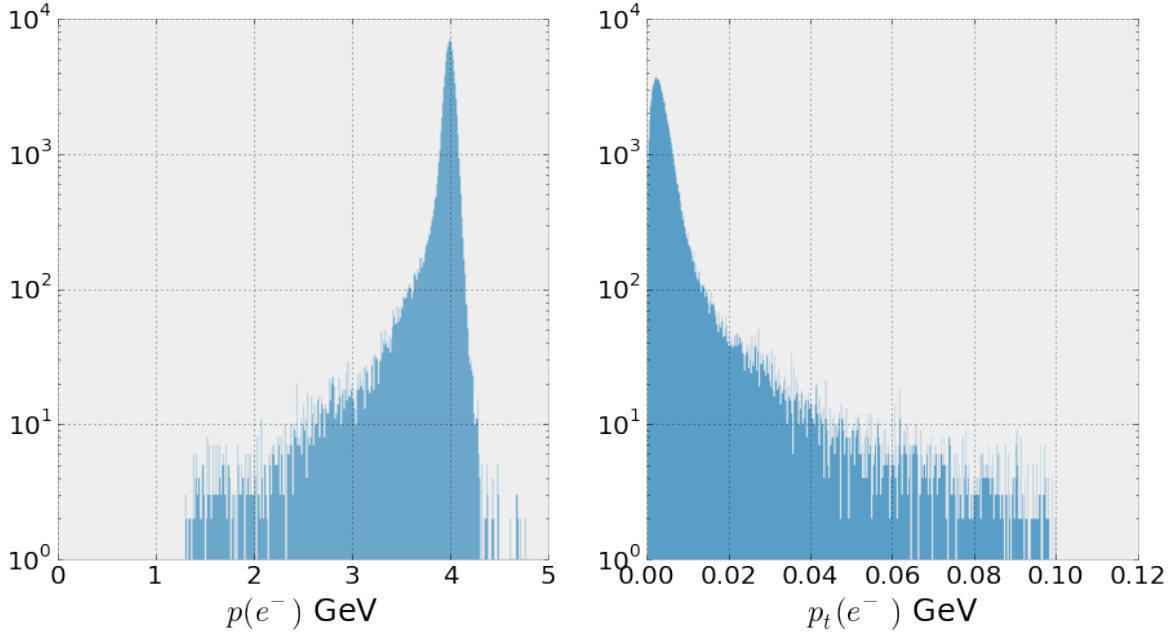
Figure 7. Reconstructed total momentum and momentum transverse to target for a sample of 4 GeV beam electrons.

Figure 8. Reconstructed Tagger track x-y position at the target for a sample of 4 GeV beam electrons.

recoil tracker. Although further study will be required to find the beam intensity limits for this tagging tracker design, we can safely conclude that it is more than capable of providing the tagging purity required for the first stage of the LDMX experiment.

5.3 Recoil Tracker Performance, (Editors: Tim Nelson, Omar Moreno)

The recoil tracker must have good efficiency for reconstructing the recoiling electrons characteristic of signal events with good resolution for transverse momentum and impact position at the target which are critical for eliminating background. In addition, the tracker should have sufficient momentum resolution that it can assist the ECal in identifying events where an incoming beam electron passes through the target and tracker without significant energy loss. Finally, the recoil tracker must help identify background events from other hard processes that can occur in the target or the tracker itself. These backgrounds include electromagnetic tridents and other events with multiple charged tracks as well as hard bremsstrahlung events where the photon undergoes a photonuclear reaction in the target or the material of the tracker.

Estimation of the recoil momentum transverse to the target requires precise determination of the angle at the target together with a good curvature measurement to set the overall momentum scale. At least two 3-d measurements directly downstream of the target are needed to determine the recoil angle while at least one additional bend-plane measurement is needed for curvature. For low-momentum
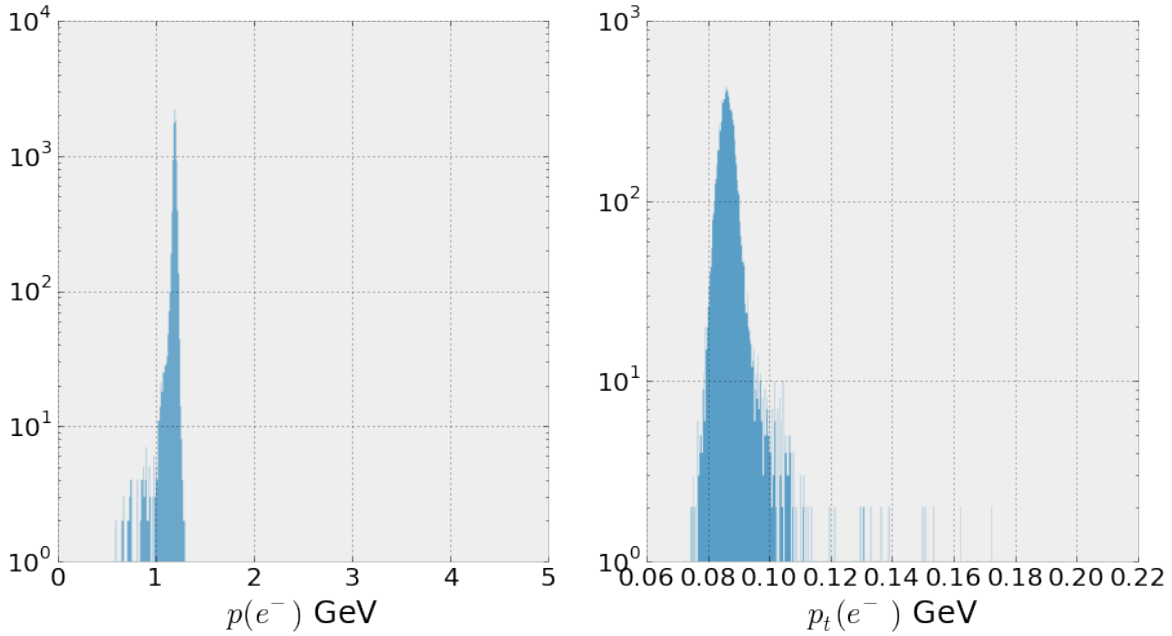
Figure 9. Reconstructed total momentum for a sample of 1.2 GeV beam electrons.

Figure 10. Reconstructed momentum vs. momentum transverse to the target for a sample of 1.2 GeV electrons in the presence of 10^{-3}, 10^{-2} and 10^{-1} random occupancy in all sensors.

tracks, this third measurement can be in the first four closely-spaced layers, but for high momentum tracks that are nearly straight, hits in both of the downstream axial layers are required. Because high-momentum signal recoils will nearly always pass through all six layers, the acceptance near the top of the energy range for signal recoils is near unity, only reduced by the single-hit efficiency in the last two layers. However, at low momentum a large number of tracks can escape detection. Therefore, in order to estimate the signal acceptance for well-measured recoils, we require that recoiling electrons leave hits in at least three of the 3-d layers, for pattern recognition and angle estimation, and at least four hits total for reasonably purity. The tracker acceptance for signal recoils as a function of mediator mass is shown in Figure XXX.

The ability to distinguish signal from background using the recoil transverse momentum is obviously limited by the multiple scattering in the target, where multiple scattering in a 10% X_0 target results in a 4 MeV smearing in transverse momentum. Using an analytic model of the target and recoil tracker, the material budget and single-hit resolutions of the recoil tracker have been designed so that the experimental resolution is limited by multiple scattering in the target over the entire momentum range for signal recoils.

5.4 Forward Electromagnetic Calorimeter (Editors: Joe Incandela)

Owen and Joe will discuss this at the July 8 meeting. But Philip's notes include:

- Hermiticity: make sure to include a study of cracks or dead material in the detector simulation. Do we need to worry about this? Why?

Large scale "top down" monte carlo study to demonstrate baseline performance of ECal and to justify more detailed study of specific reactions that dominate the tail of low energy deposition events. We need to quantify everything I'm about the say more carefully. Starting from 4×10^{14} EOT, the baseline tracker selections bring the event sample down to $\sim 4 \times 10^{12}$. So we're dealing with $\sim 4 \times 10^{12}$ events with a soft recoiling electron and a hard, ~ 3 GeV, photon. ECal events that are hadron rich occur about $\sim 10^{-3}$ of the time. So now we're down to $\sim 4 \times 10^9$ hadron rich events in the ECal.

- most importantly, we want to understand what dominates the low energy deposition events
- we want to characterize the hadron rich events (because we know they are a potential issue)
- explain veto strategy
- at what point is the energy deposition so low that it's not possible to veto effectively? what are these events types?

Specific "bottom up" studies of photo-nuclear reactions: We know that certain event types could pose a challenge, so let's study them. The numbers shown below are with very loose kinematic selections, so they are upper bounds. They are also for 9 GeV photons, so Philip and Natalia will need to correct them. This is a good starting point for study however:

- $\gamma N \to (\rho, \omega, \phi) N \to \pi^+ \pi^- N$ ($\lesssim 10^8$ of this event type).
- $\gamma N \to \mu^+ \mu^- N$ ($\lesssim 2 \times 10^7$ of this event type).
- $\gamma p \to \pi^+ n$ ($\lesssim 4 \times 10^5$ with $\sim 4 \times 10^3$ of these having a backscattered π^+).
- $\gamma n \to n \bar{n} n$ ($\lesssim 4 \times 10^5$ of this type).
- $\gamma(p, n) \to K_L K_L + X$ (expect this at the $\sim 10^3$ level, but we need to check this!)

The current plan is to use a particle gun and weight the depth of origination and angle/energy distribution using data. Let Philip and Natalia know when you're ready to do this. *We need to be especially careful to include the regions of phase space where the MIPs are soft or wide/back scattering by recoiling off the nucleons or atoms. This needs a dedicated study, starting with the physics simulations group, P,N,E,G.*

5.5 Hadronic Veto System (Editors: Jeremy Mans, Nhan Tran, Andrew Whitbeck)

The hadronic veto system is designed for detecting rare processes and therefore studies of its performance focus on "bottom up" vetoes of photo-nuclear reactions. If we consider that the rare processes described in Section **??** should produce a low multiplicity of neutrons we perform studies to compute on the efficiency the hadronic veto system of a detecting single neutron. This will give us an idea of the efficiency with which we can veto any type of photo-nuclear reaction based on the hadronic system only.

We benchmark the hadronic veto system by considering neutrons, being generated at the face of the calorimeter, with various:

- energies: 1.3, 1.5, 1.8, 2.0, 2.2, 2.5, 3.5 GeV (total energy)

- number of calorimeter layers: 15, 20, 25

- incident angles: 0, 15, 30 degrees

For each neutron phase space point, we generate 5×10^4 events.

First we study the propagation of neutrons through the HCAL purely via GEANT without yet considering the digitization of the scintillation signal, which was described in Section 4.2.2. We define the kinetic energy flux for a given layer as the amount of kinetic energy passing through the front face of a given HCAL layer. In Fig. 11, we show the neutron kinetic energy flux as a function of HCAL layer for 3.5 GeV total energy neutrons produced at an incident angle of $0.0°$. We note that the "shower max" for hadronic showers in this system is typically around layers 6/7. By looking at the neutron flux around a kinetic energy of 2.5 GeV as a function of layers, we can estimate the fraction of neutrons which pass directly through the calorimeter without interacting. We can conclude that roughly $100/50000 \sim 0.2\%$ of neutrons do not interact in the first 15 layers of the system. This number drops to roughly $0.02\%(0.002\%)$ for a 20 (25) layer system. This fraction is independent of incident neutron energy.
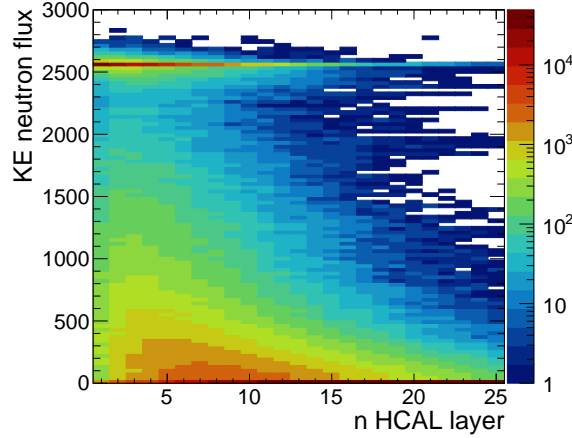

Figure 11. Neutron kinetic energy flux through the HCAL as a function of layer for a 3.5 GeV neutron produced with an incident angle of $0.0°$ at the front face of the calorimeter.

For neutrons that do interact in the HCAL, we then compute the efficiency of detecting them given a simple digitization process described in Section 4.2.2. As a reminder, we assume that a MIP deposits, on average, 1.4 MeV of energy in the scintillator, which from CMS testbeam studies we estimate translates into 13.5 photo-electrons at the SiPM. Given a typical noise contribution of 2 photo-electrons in SiPMs, we define a MIP signal in a given layer as 8 photo-electrons. Therefore, we define a *MIP layer* as a scintillator layer in the HCAL in which enough energy is deposited to produce at least 8 photo-electrons (Poisson-varied). We define a vetoed neutron event as a neutron which has created ≥ 1 MIP layer. The number of MIP layers is plotted in Fig. 12 for an incident 2.5 GeV total energy neutron assuming a system of 15, 20, or 25 layers; or in other words, counting only MIP layers in the first 15, 20, or 25 HCAL layers (left to right). In Fig. 12, we can count the number of events in the 0 bin of each plot to find the fraction of neutron events which would *not* be vetoed, which we

call *mis-vetoed* neutrons. For an incident 2.5 GeV total energy neutron, the fraction of mis-vetoed depends strongly on the number of HCAL layers in the system. This suggests, for higher energy neutrons, that the mis-veto fraction is dominated by neutrons which do not interact in the system and are not contained.
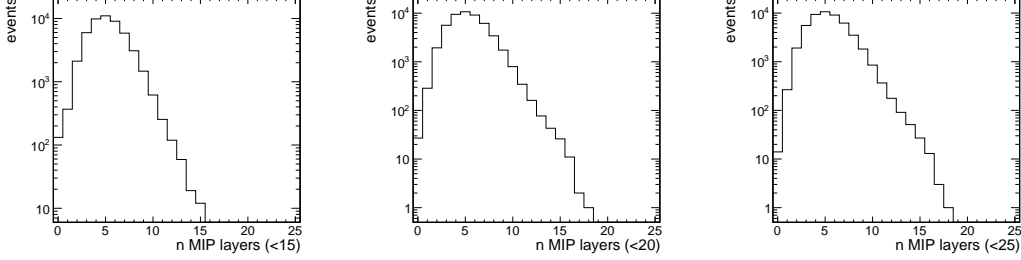

Figure 12. Number of MIP layers for a 2.5 GeV neutron produced with an incident angle of 0.0° at the front face of the calorimeter for a system of 15, 20, or 25 layers (left to right).

The number of MIP layers is plotted in Fig. 15 for an incident 1.3 GeV total energy neutron assuming a system of 15, 20, or 25 layers (left to right). Here, we note that the mis-veto efficiency is fairly constant as a function of the number of HCAL layers in the system. We conclude that most mis-vetoed neutron events for lower energy neutrons do not deposit enough energy in the scintillator to pass the threshold for a MIP layer or are directly absorbed into the Steel absorber layer.
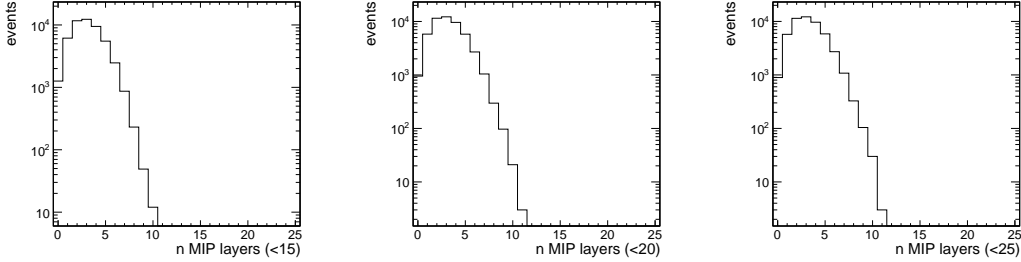

Figure 13. Number of MIP layers for a 2.5 GeV neutron produced with an incident angle of 0.0° at the front face of the calorimeter for a system of 15, 20, or 25 layers (left to right).

Finally we conclude by benchmarking performance as a function of number of layers in the system and incident neutron angle. This is shown in Fig. 14. Here we show the neutron mis-veto rate as a function of total energy, incident angle. and number of HCAL layers. First we see that the mis-veto rate fall quickly with energy which indicates that we are much more efficient at detecting higher energy neutrons at a mis-veto rate of 10^{-3}-10^{-5} depending on the number of layers in the system and the incident angle of the neutron. At higher energies, a larger incident angle or more layers reduces the mis-veto rate where in both cases the neutron traverses more material (absorber). This indicates that the main source of mis-vetoed neutrons comes neutrons that do not interact with the HCAL. For

lower energies, the mis-veto rate for neutrons is practically independent of incident angle and number of layers and is typically at a value of $10^{-}1$.
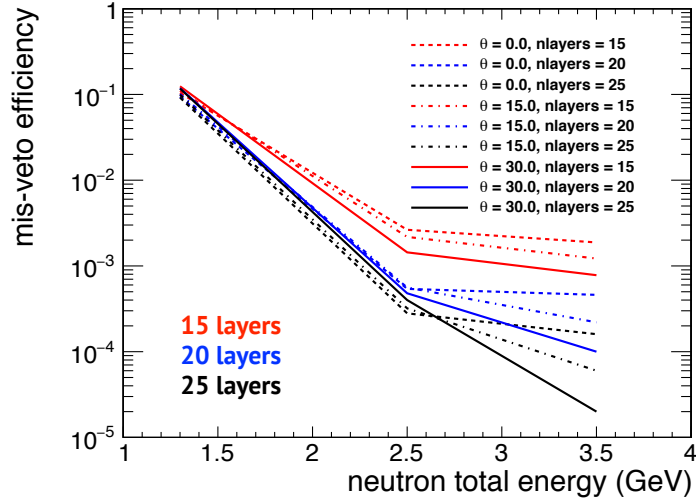

Figure 14. Number of MIP layers for a 2.5 GeV neutron produced with an incident angle of $0.0°$ at the front face of the calorimeter for a system of 15, 20, or 25 layers (left to right).

In Fig. 14, we show a more fine-grained mis-veto rate plot with more neutron energies considered.
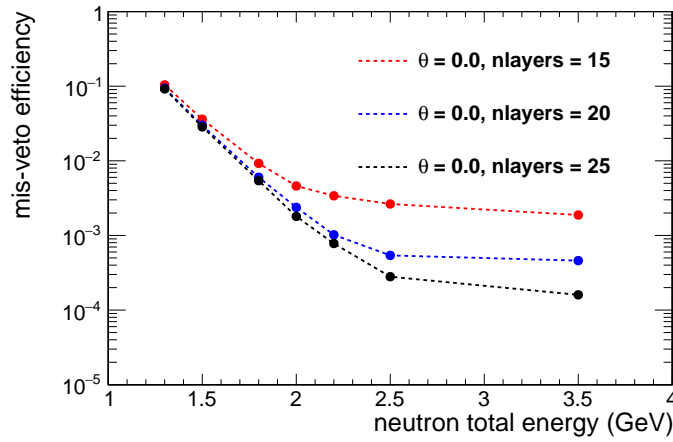

Figure 15. Number of MIP layers for a 2.5 GeV neutron produced with an incident angle of $0.0°$ at the front face of the calorimeter for a system of 15, 20, or 25 layers (left to right).

to add: studies changing absorber thickness and varying MIP layer threshold. Further studies are on-going to better improve performance at lower energies.

From single neutron studies, we conclude that we are able to veto neutrons at an event per $10^1 -$
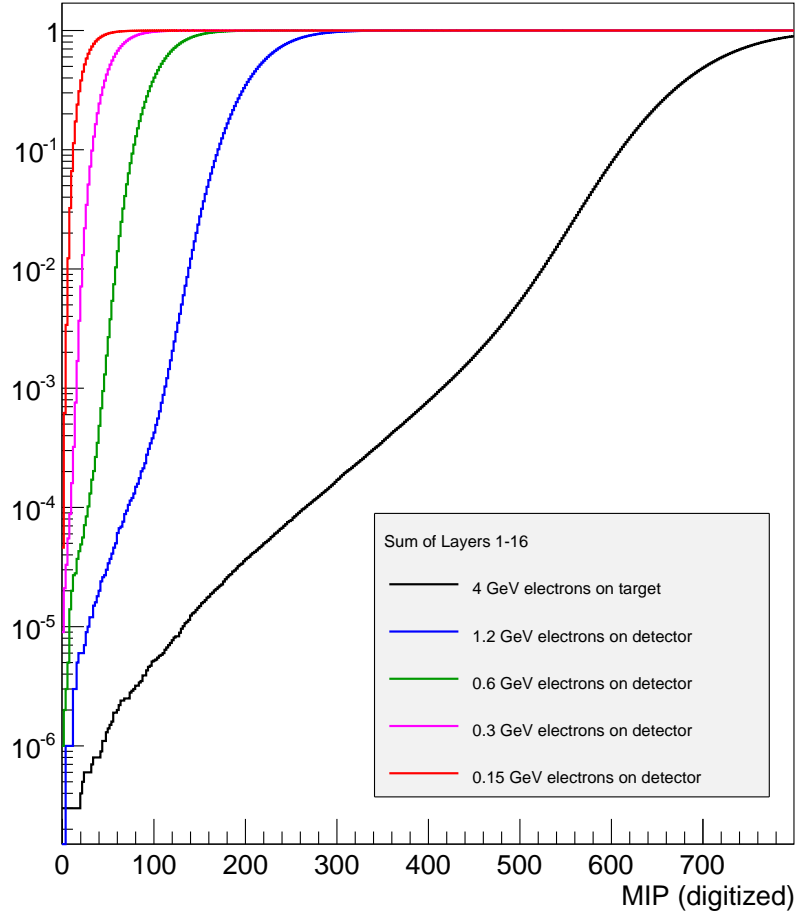
Figure 16. Performance of the primary physics trigger for LDMX. The effiency for signal electrons of differing energy and the trigger rate for all backgrounds induced by beam electrons are shown as a function of the trigger threshold in MIP units.

10^5 for neutron kinetic energies ranging from 400 MeV to 2.5 GeV depending on number of layers in the system and incident angle. In the next Section, we study in more detail the veto capabilities of the entire calorimeter system, ECAL + HCAL, for rare photo-nuclear processes.

5.6 Trigger Performance

As described above, the primary physics trigger is based on the total energy observed in the calorimeter, combined with a requirement of a single incoming electron observed in the trigger fiber hodoscope. Figure 16 shows the simulated performance of the primary physics trigger for signal and background.

Besides the primary physics trigger, the LDMX trigger system will also allow the selection of events for calibration, alignment, and background studies. The trigger will include input from the

Table 1. Draft trigger menu for LDMX, showing the primary contributions to the trigger budget for a 46 MHz beam rate

Trigger	Prescale factor	Rate (Hz)
Physics Trigger	1	
E(ECAL) < 1.2 GeV		4600
Background-Measurement Triggers		*100*
E(ECAL) > 3 GeV		25
E(ECAL) > 2 GeV		50
HCAL single MIP trigger		25
Detector-Monitoring Triggers		*50*
Beam-arrival (hodoscope)	4000000	10
Empty-detector (hodoscope veto)		10

Allocations are extremely rough at the moment!

scintillator calorimeter to allow selection of events with hadrons or muons. Each event will be marked with the set of triggers which fired. An initial draft trigger menu is shown in Table 1.

1. What is the rate of muon production? We would expect to trigger these, yes?

2. What is the impact of cosmics on the HCAL trigger?

6 Budget and Schedule

6.1 DASEL (Editors: Philip Schuster, Gordan Krnjaic)

6.2 Beamline (Editors: Tim Nelson)

6.3 Tracking (Editors: Tim Nelson, Omar Moreno)

6.4 Forward ECal (Editors: Joe Incandela, Jeremy Mans)

6.5 Hadronic Veto (Editors: Jeremy Mans, Nhan Tran, Andrew Whitbeck)

6.6 Trigger (Editors: Jeremy Mans, Nhan Tran, Andrew Whitbeck)

6.7 DAQ (Editors: Jeremy Mans, Nhan Tran, Andrew Whitbeck)

6.8 Operations